



Yashraj Bhosale¹, Tejaswin Parthasarathy¹ and Mattia Gazzola^{1,2,3,4},†

(Received 10 March 2022; revised 7 June 2022; accepted 9 June 2022)

Viscous streaming is an efficient mechanism to exploit inertia at the microscale for flow control. While streaming from rigid features has been thoroughly investigated, when body compliance is involved, as in biological settings, little is known. Here, we investigate body elasticity effects on streaming in the minimal case of an immersed soft cylinder. Our study reveals an additional streaming process, available even in Stokes flows. Paving the way for advanced forms of flow manipulation, we illustrate how gained insights may translate to complex geometries beyond circular cylinders.

Key words: microfluidics, general fluid mechanics

1. Introduction

This paper examines the role of body elasticity in two-dimensional viscous streaming. Viscous streaming (Holtsmark *et al.* 1954; Lane 1955; Bertelsen, Svardal & Tjøtta 1973), an inertial phenomenon, refers to the time-averaged, rectified steady flows that arise when an immersed body of length scale *a* undergoes small-amplitude oscillations in a viscous fluid. Long understood for rigid bodies of uniform curvature, such as cylinders (Holtsmark *et al.* 1954) or spheres (Lane 1955), viscous streaming has found application in microfluidics (Lutz, Chen & Schwartz 2003, 2005; Marmottant & Hilgenfeldt 2004; Lutz, Chen & Schwartz 2006; Wang, Jalikop & Hilgenfeldt 2011; Chong *et al.* 2013; Chen & Lee 2014; Klotsa *et al.* 2015; Thameem, Rallabandi & Hilgenfeldt 2017;

¹Mechanical Sciences and Engineering, University of Illinois at Urbana-Champaign, Urbana, IL 61801, USA

²National Center for Supercomputing Applications, University of Illinois at Urbana-Champaign, Urbana, IL 61801, USA

³Carl R. Woese Institute for Genomic Biology, University of Illinois at Urbana-Champaign, Urbana, IL 61801, USA

⁴Center for Artificial Intelligence Innovation, University of Illinois at Urbana-Champaign, Urbana, IL 61801, USA

Pommella *et al.* 2021), from chemical mixing (Liu *et al.* 2002; Lutz *et al.* 2003, 2005; Ahmed *et al.* 2009) to vesicle transport (Marmottant & Hilgenfeldt 2003, 2004), due to its ability to reconfigure flow and particle trajectories within short length – O(100) µm – and time – $O(10^{-3})$ s – scales (Thameem, Rallabandi & Hilgenfeldt 2016; Thameem *et al.* 2017). Recent developments have then furthered opportunities in transport, separation or assembly, through the use of multi-curvature bodies and associated rich flow topologies (Parthasarathy, Chan & Gazzola 2019; Bhosale, Parthasarathy & Gazzola 2020; Bhosale *et al.* 2021*b*; Chan *et al.* 2022).

Despite progress, no effort has so far systematically considered the role of body elasticity in viscous streaming. Yet, modulation by soft interfaces may be relevant in a multitude of settings, from pulsatile physiological flows (Jalal *et al.* 2018; Parthasarathy, Bhosale & Gazzola 2020; Jacob, Tingay & Leontini 2021) or conformal microfluidics (Someya, Bao & Malliaras 2016; Heikenfeld *et al.* 2018; Bandodkar *et al.* 2019) to elastic mini-robots in fluids (Park *et al.* 2016; Ceylan *et al.* 2017; Aydin *et al.* 2019; Huang *et al.* 2019), with relevance to both medicine and engineering. Soft biological organisms, such as bacteria (Spelman & Lauga 2017) or larvae (Gilpin, Bull & Prakash 2020), may also take advantage of streaming for feeding or locomotion. Indeed, a back of the envelope calculation reveals that a millimetre-size aquatic organism beating its cilia at $\sim O(10)$ Hz would operate at the edge of viscous streaming viability. Supporting this hypothesis, steady flow patterns and velocities ($\sim 10^2 - 10^3 \,\mu \text{m s}^{-1}$) consistent with streaming have been observed in starfish and ribbon-worm larvae (Gilpin *et al.* 2020), although being ascribed, perhaps inaccurately, to Stokes flow phenomena.

Motivated by these considerations, we dissect the effect of body elasticity on viscous streaming in the minimal setting of an immersed, oscillating hyperelastic circular cylinder. The major outcome is that, in these conditions, the time-averaged streaming flow $\langle \psi_1 \rangle$ reads

$$\langle \psi_1 \rangle = \sin 2\theta \left[\Theta(r) + \Lambda(r) \right], \tag{1.1}$$

where r, θ are cylindrical coordinates, $\Theta(r)$ is the classical rigid-body solution from Holtsmark *et al.* (1954) and $\Lambda(r)$ is a novel, independent contribution from body elasticity.

2. Problem set-up and governing equations

The above result is obtained by considering the set-up shown in figure 1, where a 2-D viscoelastic solid cylinder Ω_e with radius a is immersed in a viscous fluid Ω_f . The fluid oscillates with velocity $V(t) = \epsilon a\omega \cos \omega t$, where ϵ, ω and t represent the non-dimensional amplitude, angular frequency and time, respectively. We 'pin' the cylinder's centre using a rigid inclusion Γ of radius b < a, to kinematically enforce zero strain and velocity near the cylinder's centre. We denote by $\partial \Omega$ and $\partial \Gamma$ the boundary between the elastic solid and viscous fluid, and the boundary of the pinned zone, respectively.

In this set-up, we assume fluid and solid to be isotropic, incompressible and of constant density. Furthermore, we assume the fluid to be Newtonian, with kinematic viscosity v_f and density ρ_f . We assume that the solid exhibits viscoelastic Kelvin–Voigt behaviour, where the elastic stresses are modelled via neo-Hookean hyperelasticity, characteristic of soft biological materials (Bower 2009), with shear modulus G, kinematic viscosity v_e and density ρ_e . Nonetheless, as it will later become apparent, the choice of hyperelastic or viscoelastic model does not affect the general theory presented in this study. This is because in the analysis that follows, higher order nonlinear terms in the stress–strain or viscous response drop out, reducing to linear elasticity.

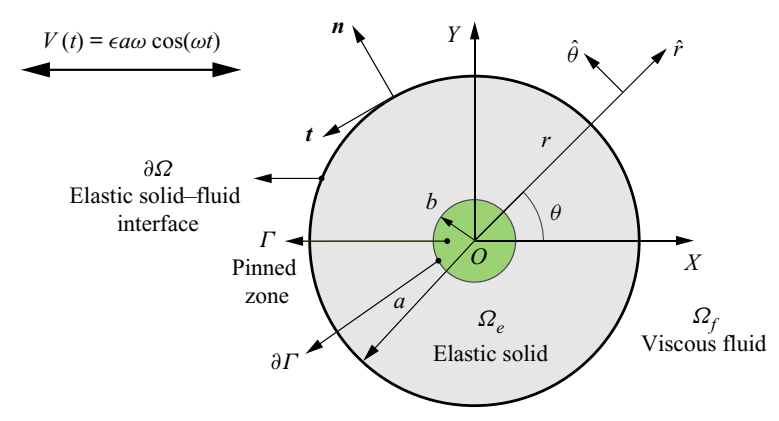


Figure 1. Problem set-up. Elastic solid cylinder Ω_e of radius a with a rigid inclusion (pinned zone Γ of radius b), immersed in the viscous fluid Ω_f . The cylinder is exposed to an oscillatory flow with far-field velocity $V(t) = \epsilon a\omega \cos(\omega t)$.

The dynamics in the elastic and fluid phases are described by the incompressible Cauchy momentum equations, non-dimensionalized using the characteristic scales of velocity $V = \epsilon a \omega$, length L = a, time $T = 1/\omega$ and hydrostatic pressure $P = \mu_f V/L = \mu_f \epsilon \omega$:

Incomp.
$$\left\{ \nabla \cdot \boldsymbol{v} = 0, \ \boldsymbol{x} \in \Omega_{f} \cup \Omega_{e} \right.$$

$$\left. \text{Fluid} \left\{ \frac{\partial \boldsymbol{v}}{\partial t} + \epsilon(\boldsymbol{v} \cdot \nabla)\boldsymbol{v} = \frac{1}{M^{2}} \left(-\nabla p + \nabla^{2}\boldsymbol{v} \right), \ \boldsymbol{x} \in \Omega_{f} \right.$$

$$\left. \text{Solid} \left\{ \alpha \text{Cau} \left(\frac{\partial \boldsymbol{v}}{\partial t} + \epsilon(\boldsymbol{v} \cdot \nabla)\boldsymbol{v} \right) = \frac{\text{Cau}}{M^{2}} \left(-\nabla p + \beta \nabla^{2}\boldsymbol{v} \right) + \nabla \cdot (\boldsymbol{F}\boldsymbol{F}^{T})', \ \boldsymbol{x} \in \Omega_{e}, \right.$$

$$\left. (2.1) \right.$$

where v and p are the velocity and pressure fields, and F is the deformation gradient tensor, defined as $F = I + \nabla u$, where I is the identity, u = x - X is the material displacement field and x, X are the position of a material point after deformation and at rest, respectively. The prime symbol ' on a tensor denotes its deviatoric. In addition, the following non-dimensional groups naturally appear: scaled oscillation amplitude ϵ , Womersley number $M = a\sqrt{\rho_f \omega/\mu_f}$, Cauchy number $Cau = \epsilon \rho_f a^2 \omega^2/G$, density ratio $\alpha = \rho_e/\rho_f$ and viscosity ratio $\beta = \mu_e/\mu_f$. Physically, M represents the ratio of inertial to viscous forces, and Cau represents the ratio of inertial to elastic forces. Thus, increasing M indicates an inertia-dominated environment, and increasing Cau implies a softer body. The equations are then closed using the boundary conditions

Pinned zone
$$\{u = 0, v = 0, x \in \Gamma,$$
 (2.2)

Interface velocity
$$\left\{ \mathbf{v}_e = \mathbf{v}_f, \ \mathbf{x} \in \partial \Omega, \right.$$
 (2.3)

Interface stresses
$$\begin{cases} \sigma_{f} = -pI + (\nabla v + \nabla v^{T}), \ x \in \Omega_{f}, \\ \sigma_{e} = -pI + \beta(\nabla v + \nabla v^{T}) + \frac{M^{2}}{\operatorname{Cau}}(FF^{T})', \ x \in \Omega_{e}, \\ n \cdot \sigma_{e} \cdot n = n \cdot \sigma_{f} \cdot n, \ x \in \partial \Omega, \\ n \cdot \sigma_{e} \cdot t = n \cdot \sigma_{f} \cdot t, \ x \in \partial \Omega, \end{cases}$$
(2.4)

Y. Bhosale, T. Parthasarathy and M. Gazzola

Far-field
$$\left\{ v(|x| \to \infty) = \cos \omega t \, \hat{i}, \ x \in \Omega_f, \right.$$
 (2.5)

where (2.2) is the rigid pin constraint, (2.3) is the no-slip condition, (2.4) enforces continuity of stresses and (2.5) is the far-field flow. We note the use of subscripts e and f to explicitly denote elastic and fluid phases whenever ambiguity may arise, particularly in treating interfacial quantities. Next, we identify relevant parameter ranges and solve (2.1) accordingly, using perturbation theory.

3. Perturbation series solution

Typically, in viscous streaming applications, the non-dimensional oscillation amplitude is $\epsilon \ll 1$ (Holtsmark et~al.~1954; Bertelsen et~al.~1973; Lutz et~al.~2005), and the Womersley number is $M \geq O(1)$ (Marmottant & Hilgenfeldt 2004; Lutz et~al.~2006). Additionally, density α and viscosity β ratios are $\sim O(1)$. The Cauchy number Cau requires careful consideration. For a rigid body Cau = 0, while for an elastic body Cau > 0, with Cau $\ll 1$ implying weak elasticity. From a mathematical perspective, dealing with Cau $\geq O(1)$ is challenging due to the highly nonlinear nature of hyperelastic materials. Here, we assume that the cylinder is only weakly elastic, and in particular that Cau $= \kappa \epsilon$, where $\kappa = O(1)$. This assumption simplifies the asymptotic treatment, slaving Cau to ϵ so that both are equally small and tend to zero at the same rate. As further discussed in the supplementary material, § 2 available at https://doi.org/10.1017/jfm.2022.525, this modelling choice does not compromise the practical generality of our findings.

We then look for asymptotic solutions of (2.1) by perturbing all relevant fields as series of powers of ϵ . We derive the zeroth-order solution O(1), which reduces to a rigid cylinder in a purely oscillatory flow governed by the unsteady Stokes equation (Holtsmark *et al.* 1954). The next-order solution $O(\epsilon)$ is derived in two steps. First, we obtain the deformation of the elastic solid due to the leading-order flow. Second, we use this deformation to determine the boundary conditions for the flow at $O(\epsilon)$, thus incorporating elasticity effects into the streaming solution. Steps are mathematically outlined below, with details in the supplementary material.

We start by perturbing to $O(\epsilon)$ all physical quantities q, which include v, u, p, Ω , n, t, as

$$q \sim q_0 + \epsilon q_1 + O\left(\epsilon^2\right) \tag{3.1}$$

and substitute them in (2.1). Subscripts (0, 1, ...) indicate the solution order. Then, we adopt the more convenient cylindrical coordinate system (r, θ) , with radial coordinate r, angular coordinate θ and origin at the centre of the cylinder. Horizontal axis direction i corresponds to $\theta = 0$.

3.1. Zeroth-order
$$O(1)$$
 solution

At zeroth order O(1), the governing equations and boundary conditions in the solid reduce to

$$\nabla \cdot ((I + \nabla u_0)(I + \nabla u_0)^{\mathrm{T}})' = 0, \quad r \le 1; \ u_0|_{r=\zeta} = 0, \tag{3.2}$$

where $\zeta = b/a$ is the non-dimensional radius of the pinned zone. Since at this order Cau = $\kappa \epsilon = 0$, the solution of (3.2) is the fixed, rigid body cylinder:

$$\partial \Omega_0 = r = 1; \quad \mathbf{u}_0 = 0, \quad \mathbf{v}_0 = \frac{\partial \mathbf{u}_0}{dt} = 0, \quad r \le 1.$$
 (3.3)

With these zeroth-order definitions, the governing equations in the fluid reduce to

$$M^{2} \frac{\partial \nabla^{2} \psi_{0}}{\partial t} = \nabla^{4} \psi_{0} \quad r \ge 1,$$

$$v_{0,r}|_{r=1} = \frac{1}{r} \frac{\partial \psi_{0}}{\partial \theta} \Big|_{r=1} = 0; \quad v_{0,\theta}|_{r=1} = -\frac{\partial \psi_{0}}{\partial r} \Big|_{r=1} = 0,$$

$$v_{0,r}|_{r \to \infty} = \cos \theta \cos t; \quad v_{0,\theta}|_{r \to \infty} = -\sin \theta \cos t,$$

$$(3.4)$$

where ψ is the streamfunction defined as $\mathbf{v} = \nabla \times \psi$. This system ((3.3) and (3.4)) is a rigid cylinder immersed in an oscillating unsteady Stokes flow, which has the exact analytical solution (Holtsmark *et al.* 1954)

$$\psi_0 = \frac{\sin \theta}{2} \left(r + \frac{H_2(m)}{rH_0(m)} - \frac{2H_1(mr)}{mH_0(m)} \right) e^{-it} + \text{c.c.}, \ r \ge 1,$$
 (3.5)

where $i = \sqrt{-1}$, and $m = \sqrt{i}M$. Here, H_i and c.c. refer to the *i*th-order Hankel function of first kind and complex conjugate. The zeroth-order field ψ_0 in the fluid is purely oscillatory, thus no steady streaming is observed at O(1), as expected (Holtsmark *et al.* 1954; Bertelsen *et al.* 1973). Additionally, no effects of elasticity manifest on the flow at this order.

3.2. First-order $O(\epsilon)$ solution

We then proceed to the next order of approximation $O(\epsilon)$, where we instead do expect steady streaming to emerge and elasticity to play a role. At $O(\epsilon)$, the solid governing equations reduce (supplementary material, (1.42), (1.49)) to

$$\nabla^4 \psi_{e,1} = 0, \quad x \in \Omega_e, \tag{3.6}$$

where we have defined the strain function ψ_e , so that $u = \nabla \times \psi_e$ (similar to the streamfunction ψ). Equation (3.6) shows how the specific choice of solid elasticity model is irrelevant at $O(\epsilon)$, since all nonlinear stress-strain responses drop out due to linearization (supplementary material, (1.37)–(1.42)). Equation (3.6) is further complemented by the boundary conditions at the pinned zone interface:

$$u_{1,r} = \frac{1}{r} \frac{\partial \psi_{e,1}}{\partial \theta} \bigg|_{r=r} = 0; \quad u_{1,\theta} = -\frac{\partial \psi_{e,1}}{\partial r} \bigg|_{r=r} = 0. \tag{3.7a,b}$$

Now, the flow solution at O(1) exerts interfacial stresses on the solid, which at $O(\epsilon)$ is no longer rigid but instead deforms. This process is driven by (2.4), which yields the following radial and tangential stress conditions:

$$\frac{M^{2}}{\kappa} \left. \frac{\partial}{\partial r} \left(\frac{1}{r} \frac{\partial \psi_{e,1}}{\partial \theta} \right) \right|_{r=1} = \left. \frac{\partial v_{0,r}}{\partial r} \right|_{r=1},$$

$$\frac{M^{2}}{\kappa} \left(\frac{1}{r^{2}} \frac{\partial^{2} \psi_{e,1}}{\partial \theta^{2}} - \frac{\partial^{2} \psi_{e,1}}{\partial r^{2}} + \frac{1}{r} \frac{\partial \psi_{e,1}}{\partial r} \right) \right|_{r=1} = \left. \left(\frac{1}{r} \frac{\partial v_{0,r}}{\partial \theta} + \frac{\partial v_{0,\theta}}{\partial r} - \frac{v_{0,\theta}}{r} \right) \right|_{r=1},$$
(3.8)

where the left-hand side corresponds to the elastic stresses in the solid phase $((M^2/\text{Cau})(FF^T)', (2.4))$ and the right-hand side to the viscous stresses in the fluid phase

 $(\nabla v + \nabla v^T, (2.4))$, both evaluated at the zeroth-order interface r = 1. We note that the pressure term (-pI, (2.4)) cancels out from both sides of (3.8), since at O(1) the pressure is continuous at the interface (supplementary material, (1.31)). Additionally, (3.8) shows how the choice of solid viscosity model is irrelevant at $O(\epsilon)$, since the solid viscosity term $(\beta(\nabla v + \nabla v^T), (2.4))$ is of order higher than $O(\epsilon)$, and thus drops out (supplementary material, (1.37)–(1.42)). We further note that although the solid interface does deform, the use of r = 1 in (3.8) is not inconsistent. Indeed, as shown in the supplementary material ((1.44)–(1.46)), this approximation induces higher order $O(\epsilon^2)$ errors in the boundary stresses evaluation. The flow quantities on the right-hand side can be then directly evaluated:

$$\frac{\partial v_{0,r}}{\partial r}\Big|_{r=1} = 0,$$

$$\left(\frac{1}{r}\frac{\partial v_{0,r}}{\partial \theta} + \frac{\partial v_{0,\theta}}{\partial r} - \frac{v_{0,\theta}}{r}\right)\Big|_{r=1} = \sin\theta F(m) e^{-it} + \text{c.c.},$$
(3.9)

with

$$F(m) = -mH_1(m)/H_0(m). (3.10)$$

Once (3.9) and (3.10) are substituted back in the boundary conditions of (3.8), the biharmonic (3.6) can be solved to obtain the $O(\epsilon)$ solid displacement field:

$$\psi_{e,1} = \frac{\kappa}{M^2} \sin \theta(r) \left(c_1 + \frac{c_2}{r^2} + c_3 r^2 + c_4 \ln(r) \right) F(m) e^{-it} + \text{c.c.}, \tag{3.11}$$

where the expressions for c_1 , c_2 , c_3 , c_4 (functions of ζ) are reported in the supplementary material. Equation (3.11) represents the $O(\epsilon)$ solid displacement field both in the bulk Ω_e and at the boundary $\partial \Omega$, which directly affects the $O(\epsilon)$ flow. At $O(\epsilon)$, the flow governing equation, in streamfunction form, reads (Holtsmark *et al.* 1954)

$$M^{2} \frac{\partial \nabla^{2} \psi_{1}}{\partial t} + M^{2} \left((\boldsymbol{v}_{0} \cdot \boldsymbol{\nabla}) \nabla^{2} \psi_{0} \right) = \nabla^{4} \psi_{1}, \quad r \ge 1.$$
 (3.12)

Since we are interested in steady streaming, we consider the time average:

$$\nabla^{4} \langle \psi_{1} \rangle = M^{2} \underbrace{\langle (\boldsymbol{v}_{0} \cdot \nabla) \nabla^{2} \langle \psi_{0} \rangle \rangle}_{\text{right-hand side}}, \quad r \geq 1, \tag{3.13}$$

where the right-hand side can be rewritten using (3.5) to yield

$$\nabla^{4} \langle \psi_{1} \rangle = \sin 2\theta \ \rho(r), \quad r \ge 1,$$

$$\rho(r) = -\frac{M^{4}}{2} \operatorname{Im} \left[\frac{H_{2}(mr)}{H_{0}(m)} + \frac{H_{2}(m)H_{0}^{*}(mr)}{H_{0}^{2}(m)r^{2}} + 2\frac{H_{0}(mr)H_{2}^{*}(mr)}{H_{0}^{2}(m)} \right],$$
(3.14)

with $Im[\cdot]$ representing the imaginary part. To solve this equation, we first recall the far-field boundary conditions:

$$\frac{1}{r} \frac{\partial \langle \psi_1 \rangle}{\partial \theta} \bigg|_{r \to \infty} = \left. \frac{\partial \langle \psi_1 \rangle}{\partial r} \right|_{r \to \infty} = 0. \tag{3.15}$$

Next, we recall the no-slip boundary condition of (2.3) that needs to be enforced at the $O(\epsilon)$ accurate solid–fluid interface (supplementary material, (1.62))

$$\mathbf{v}_{e}|_{\partial\Omega} = \mathbf{v}_{e}|_{r=1+\epsilon u_{1,r}} + O\left(\epsilon^{2}\right) = \mathbf{v}_{f}|_{\partial\Omega} = \mathbf{v}_{f}|_{r=1+\epsilon u_{1,r}} + O\left(\epsilon^{2}\right),$$
 (3.16)

where we highlight how, at $O(\epsilon)$, the cylinder interface is no longer fixed at r=1, but deforms as $r'=1+\epsilon u_{1,r}$. Here, $u_{1,r}$ is the $O(\epsilon)$ accurate deformation field computed by

injecting (3.11) into $u_1 = \nabla \times \psi_{e,1}$. To enforce (3.16), while maintaining an analytically tractable formulation, we replace the boundary flow velocity $v_f|_{r=r'}$ on the temporally moving interface r' with the velocity that the flow would need to see on the fixed interface r=1 to respond equivalently. We achieve this (supplementary material, (1.64)–(1.66)) by Taylor expanding $v_f|_{r=r'}$ around r=1:

$$\mathbf{v}_f \Big|_{r=1+\epsilon u_{1,r}} = \left(\epsilon \mathbf{v}_{f,1} + \epsilon \frac{\partial \mathbf{v}_{f,0}}{\partial r} u_{1,r} \right) \Big|_{r=1} + O\left(\epsilon^2 \right). \tag{3.17}$$

Similarly, $v_e|_{r=1+\epsilon u_{1,r}}$ (left-hand side of (3.16)) can be computed to $O(\epsilon)$ accuracy as $\partial u_{1,r}/\partial t|_{r=1}$ (supplementary material, (1.63)). Given that $u_{1,r}$ (3.11) and $\partial v_{f,0}/\partial r$ (3.5) are known, we can plug (3.17) into (3.16) to obtain $v_{f,1}$ (supplementary material, (1.62)–(1.67)), referred to as v_1 henceforth. Time averaging yields

$$\langle v_{1,r} \rangle \Big|_{r=1} = \frac{1}{r} \frac{\partial \langle \psi_1 \rangle}{\partial \theta} \Big|_{r=1} = 0,$$

$$-\langle v_{1,\theta} \rangle \Big|_{r=1} = \frac{\partial \langle \psi_1 \rangle}{\partial r} \Big|_{r=1} = \frac{\kappa}{M^2} \sin 2\theta \ G_1(\zeta) F(m) F^*(m)$$
(3.18)

with

$$G_1(\zeta) = 0.5 \left(\frac{(\zeta^2 + 1)ln(\zeta)}{\zeta^2 - 1} - 1 \right).$$
 (3.19)

Equation (3.18) tells us that, from the fluid perspective, the no-slip condition on the moving interface r' can be equivalently seen as a rectified tangential slip velocity $(\langle v_{1,\theta} \rangle|_{r=1} \neq 0)$ on the zeroth order, fixed interface r=1 (for details, see supplementary material, (1.62)–(1.67)). In our case, this slip velocity stems from solid elasticity and modifies the Reynolds stresses – $\sin 2\theta \ \rho(r)$ – associated with the rigid body (3.14), thus altering the overall streaming flow response. We remark that this slip is independent of the Navier–Stokes nonlinear inertial advection. Hence, streaming can be generated even in the Stokes limit, unlike for rigid bodies. This is similar, in spirit, to the mixed-mode streaming of pulsating bubbles (Longuet-Higgins 1998; Spelman & Lauga 2017), with the difference that in our treatment, this effect naturally emerges from the fully coupled interaction between the elastic solid and the primary flow.

Given the steady flow of (3.14) and boundary conditions of (3.15) and (3.18), the streaming solution can finally be written as

$$\langle \psi_1 \rangle = \sin 2\theta \ [\Theta(r) + \Lambda(r)].$$
 (3.20)

Here, $\Theta(r)$ is the classical rigid body contribution from (Holtsmark *et al.* 1954):

$$\Theta(r) = -\frac{r^4}{48} \int_r^{\infty} \frac{\rho(\tau)}{\tau} d\tau + \frac{r^2}{16} \int_r^{\infty} \tau \rho(\tau) d\tau
+ \frac{1}{16} \left(\int_1^r \tau^3 \rho(\tau) d\tau + \int_1^{\infty} \frac{\rho(\tau)}{\tau} d\tau - 2 \int_1^{\infty} \tau \rho(\tau) d\tau \right)
+ \frac{1}{r^2} \left(-\frac{1}{48} \int_1^r \tau^5 \rho(\tau) d\tau - \frac{1}{24} \int_1^{\infty} \frac{\rho(\tau)}{\tau} d\tau + \frac{1}{16} \int_1^{\infty} \tau \rho(\tau) d\tau \right), \quad (3.21)$$

where τ is the radial coordinate, and $\Lambda(r)$ is the new elastic modification

$$\Lambda(r) = 0.5 \frac{\kappa}{M^2} G_1(\zeta) F(m) F^*(m) \left(1 - \frac{1}{r^2} \right), \tag{3.22}$$

with $G_1(\zeta)$ and F(m) given in (3.19) and (3.10). This concludes our theoretical analysis.

Y. Bhosale, T. Parthasarathy and M. Gazzola

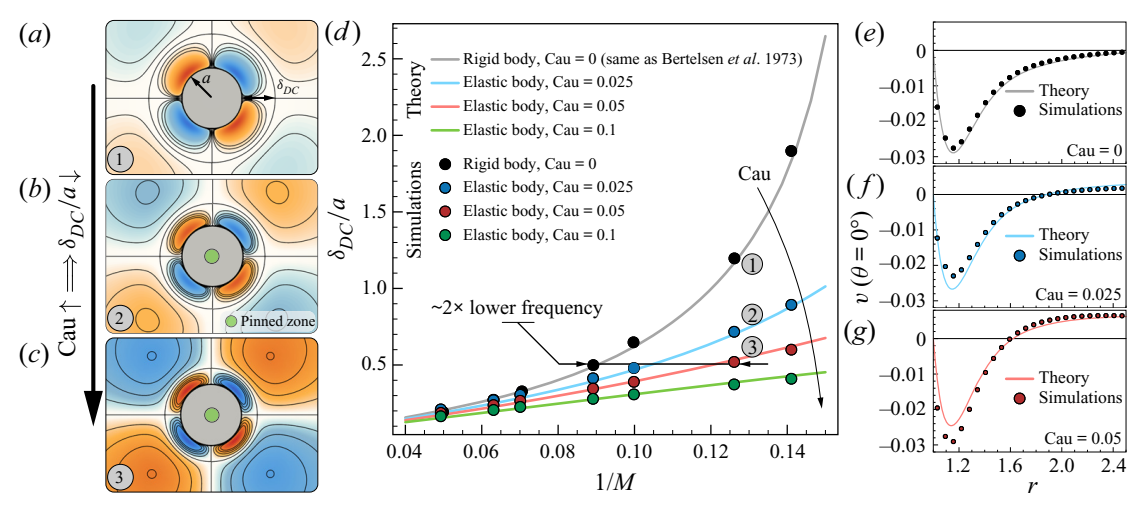


Figure 2. Effect of elasticity on streaming flow. (a-c) Time-averaged Lagrangian (i.e. Stokes-drift corrected – see supplementary material, § 3 for details) streamline patterns (blue/orange represent clockwise/anticlockwise rotating regions) depicting streaming response at $M \approx 8$ with increasing softness Cau: (a) rigid limit (Cau = 0), (b) Cau = 0.025 and (c) Cau = 0.05. Non-dimensional radius of the pinned zone (green cylinder) is set at $\zeta = 0.2$ throughout the study. For effects of ζ variation on streaming, refer to supplementary material, § 5. (d) Normalized DC layer thickness δ_{DC}/a vs inverse of Womersley number (1/M) from theory and simulations, for varying body elasticity Cau. The DC layer is the innermost recirculation zone (a-c). Its extent (finite or infinite thickness) and flow velocities characterize streaming. Its robust nature and high flow gradients and curvatures render the DC layer useful for trapping, filtration or chemical mixing. (e-g) Radial decay of velocity magnitude along $\theta = 0^{\circ}$ from theory and simulations, with increasing softness Cau. Experimental parameter values equivalent to the range of M and Cau considered here can be found in supplementary material, § 6, revealing practical viability in association with soft tissue or common polymeric materials. Simulations are performed using a remeshed vortex methodology (Gazzola et al. 2011; Bhosale, Parthasarathy & Gazzola 2021a) that accurately solves the vorticity-velocity formulation of the Navier-Stokes equations. The flow domain is discretized as particles for vorticity advection. The vorticity carried by particles is then interpolated on a regular mesh for the evaluation of all other terms. Within this framework, the rigid cylinder is modelled as a density matched ($\rho_f = \rho_e = 1$) Brinkmann solid, while the elastic cylinder is modelled as a density matched viscoelastic Kelvin-Voigt solid with shear modulus G. Deformations are tracked using an inverse-map technique (Kamrin & Nave 2009; Kamrin, Rycroft & Nave 2012). The pinned zone is modelled as a Brinkmann solid. The parametric values for the far-field motion $V(t) = V_0 \cos \omega t$ with characteristic velocity $V_0 = \epsilon a\omega$, are $\epsilon = 0.1$ and $\omega = 32\pi$. Parametric values of fluid dynamic viscosity μ_f , oscillation frequency ω and shear modulus G are determined based on the Womersley number $M = a\sqrt{\rho_f \omega/\mu_f}$, and Cauchy number Cau = $\epsilon \rho_f a^2 \omega^2 / G$. Additional simulation details: domain $[0, 1]^2$, uniform grid spacing h = 1/1024, penalization factor $\lambda = 1 \times 10^4$, mollification length $\epsilon_{moll} = 2\sqrt{2}h$, Lagrangian Courant–Friedrichs–Lewy number LCFL = 0.1. These values are used throughout the text, unless stated otherwise. Refer to Gazzola et al. (2011) and Bhosale et al. (2021a) for details on these parameters.

4. Numerical validation and extension to bodies of multiple curvatures

Next, we compare our theory against known analytical results in the rigidity limit (Raney, Corelli & Westervelt 1954; Bertelsen *et al.* 1973), and direct numerical simulations performed using remeshed vortex methods (Bhosale *et al.* 2021*a*; Gazzola, Van Rees & Koumoutsakos 2012) (see also the caption of figure 2). For a rigid cylinder (Cau = 0) oscillating at $M \approx 8$, numerical time-averaged Lagrangian streamlines (i.e. Stokes-drift corrected – see supplementary material, § 3 for details) are shown in figure 2(*a*). We highlight the fourfold symmetry and the presence of a well-defined direct circulation (DC) layer of thickness δ_{DC} . Holtsmark *et al.* (1954) predict this flow topology, as well as an increase of δ_{DC} with 1/M until divergence, at which point the DC layer extends to infinity. This behaviour is recovered by our theory when Cau = 0 (i.e. Λ = 0), and by simulations

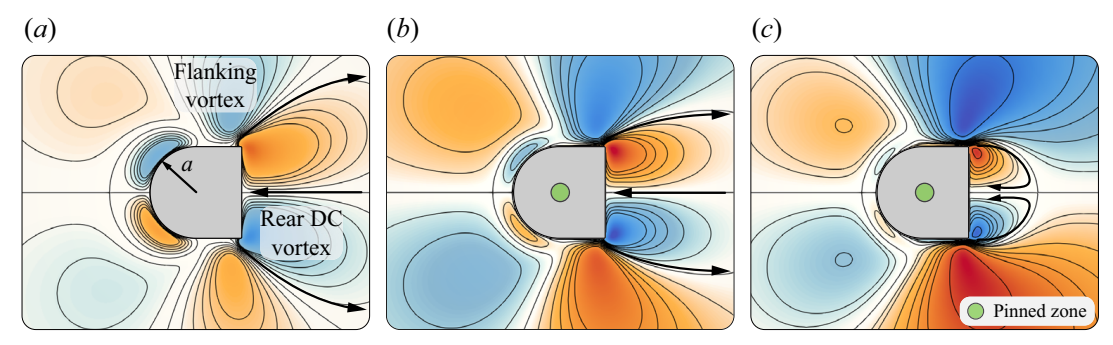


Figure 3. Extension of compliance-induced streaming to generalised, multiple curvature bodies. Time-averaged Eulerian flow topologies obtained from simulations for a bullet – formed by hybridizing a circle of radius a with a square of side length 2a – at $M \approx 8$, with varying body elasticity Cau: (a) rigid limit Cau = 0, (b) Cau = 0.05 and (c) Cau = 0.1. Increasing body softness results in contraction and strengthening of the rear DC vortex on the square side, consistent with our theoretical insights.

(black line/dots in figure 2d). As the cylinder becomes soft (Cau > 0), fourfold symmetry is preserved (sin 2θ in (3.20)), but δ_{DC} contracts on account of the elastic term $\Lambda \neq 0$. This is confirmed by simulations across a range of Cau, as seen in figure 2(b-d). An intuitive argument for this effect may be the following. If the cylinder is soft (Cau > 0), its surface deforms and the associated deformation velocities feed back into the flow, acting as an additional source of inertia. As a result, the flow effectively 'sees' a greater M relative to the rigid case, hence a decrease of DC layer thickness with elasticity (Cau). This further implies that an elastic body can access the streaming flow configurations of rigid objects with significantly lower oscillation frequencies. This can be seen in figure 2(d), where, for example at Cau = 0.05, a $\sim 2 \times$ frequency reduction is observed. Additionally, we note that for soft cylinders the divergence of δ_{DC} with decreasing M is still expected as for rigid counterparts, although at lower values of M. This is because for Cau > 0, the rigid body contribution $\Theta(r)$ is the same as in classic streaming and will diverge, with the elasticity contribution $\Lambda(r)$ only shifting the curve (see supplementary material, § 7 for details). We conclude our validation by reporting in figure 2(e-g) theoretical and simulated radially varying, time-averaged velocities $|\langle v \rangle|$ at $\theta = 0^{\circ}$, noting close agreement. For a detailed analysis surrounding the effect of inertia (M) and elasticity (Cau) on velocity magnitudes (flow strength), the reader is referred to § 4 of supplementary material.

Finally, we demonstrate how gained theoretical intuition extends to geometries of multiple curvatures. We consider the shape of figure 3, previously designed (Bhosale *et al.* 2020) to attain streaming flows favourable to particle transport (Parthasarathy *et al.* 2019) and separation (Bhosale *et al.* 2021b). Both applications rely on the presence of flanking and rear vortices, and performance is improved by strengthening the vortices via increasing oscillation frequencies (Bhosale *et al.* 2020). Figure 3 shows how the same process can alternatively be achieved by increasing softness only. As a result, the same flow topologies of Bhosale *et al.* (2020) are obtained in figure 3 for frequencies \sim 4× lower.

5. Conclusion

In summary, we derived a viscous streaming theory for the case of an elastic cylinder, and validated it computationally. Our study reveals an additional, tunable mode of streaming, accessible through material compliance and available even in Stokes flow. We demonstrate its use for flow control in the case of a previously designed streaming body of multiple curvatures, to illustrate application potential in microfluidics or microrobotics,

Y. Bhosale, T. Parthasarathy and M. Gazzola

in conjunction with the use of elastomeric or biological materials. Further, the fact that compliance enables streaming effects at frequencies significantly lower than rigid bodies supports the hypothesis that biological creatures, speculated to operate at the edge of viscous streaming viability, may instead take full advantage of it thanks to their softness.

Supplementary material. Supplementary material is available at https://doi.org/10.1017/jfm.2022.525.

Acknowledgements. We thank S. Agarwal, S. Hilgenfeldt and M. Matalon for helpful discussions over the course of this work.

Funding. The authors acknowledge support by the National Science Foundation under NSF CAREER grant no. CBET-1846752 (MG). This work used the Extreme Science and Engineering Discovery Environment (XSEDE) (Towns *et al.* 2014) Stampede2, supported by National Science Foundation grant no. ACI-1548562, at the Texas Advanced Computing Center (TACC) through allocation TG-MCB190004.

Declaration of interests. The authors report no conflict of interest.

Author ORCIDs.

Mattia Gazzola https://orcid.org/0000-0003-2129-379X.

REFERENCES

- AHMED, D., MAO, X., JULURI, B.K. & HUANG, T.J. 2009 A fast microfluidic mixer based on acoustically driven sidewall-trapped microbubbles. *Microfluid. Nanofluid.* 7 (5), 727–731.
- AYDIN, O., ZHANG, X., NUETHONG, S., PAGAN-DIAZ, G.J., BASHIR, R., GAZZOLA, M. & SAIF, M.T.A. 2019 Neuromuscular actuation of biohybrid motile bots. *Proc. Natl Acad. Sci.* 116 (40), 19841–19847.
- BANDODKAR, A.J., et al. 2019 Battery-free, skin-interfaced microfluidic/electronic systems for simultaneous electrochemical, colorimetric, and volumetric analysis of sweat. Sci. Adv. 5 (1), eaav3294.
- BERTELSEN, A., SVARDAL, A. & TJØTTA, S. 1973 Nonlinear streaming effects associated with oscillating cylinders. *J. Fluid Mech.* **59** (3), 493–511.
- BHOSALE, Y., PARTHASARATHY, T. & GAZZOLA, M. 2020 Shape curvature effects in viscous streaming. J. Fluid Mech. 898, A13.
- BHOSALE, Y., PARTHASARATHY, T. & GAZZOLA, M. 2021a A remeshed vortex method for mixed rigid/soft body fluid–structure interaction. *J. Comput. Phys.* 444, 110577.
- BHOSALE, Y., VISHWANATHAN, G., PARTHASARATHY, T., JUAREZ, G. & GAZZOLA, M. 2021b Multi-curvature viscous streaming: flow topology and particle manipulation. arXiv:2111.07184.
- BOWER, A.F. 2009 Applied Mechanics of Solids. CRC Press.
- CEYLAN, H., GILTINAN, J., KOZIELSKI, K. & SITTI, M. 2017 Mobile microrobots for bioengineering applications. *Lab on a Chip* 17 (10), 1705–1724.
- CHAN, F.K., BHOSALE, Y., PARTHASARATHY, T. & GAZZOLA, M. 2022 Three-dimensional geometry and topology effects in viscous streaming. *J. Fluid Mech.* **933**, A53.
- CHEN, Y. & LEE, S. 2014 Manipulation of biological objects using acoustic bubbles: a review. *Integr. Compar. Biol.* **54** (6), 959–968.
- CHONG, K., KELLY, S.D., SMITH, S. & ELDREDGE, J.D. 2013 Inertial particle trapping in viscous streaming. *Phys. Fluids* **25** (3), 033602.
- GAZZOLA, M., CHATELAIN, P., VAN REES, W.M. & KOUMOUTSAKOS, P. 2011 Simulations of single and multiple swimmers with non-divergence free deforming geometries. *J. Comput. Phys.* **230** (19), 7093–7114.
- GAZZOLA, M., VAN REES, W.M. & KOUMOUTSAKOS, P. 2012 C-start: optimal start of larval fish. *J. Fluid Mech.* 698, 5–18.
- GILPIN, W., BULL, M.S. & PRAKASH, M. 2020 The multiscale physics of cilia and flagella. *Nat. Rev. Phys.* 2 (2), 74–88.
- HEIKENFELD, J., JAJACK, A., ROGERS, J., GUTRUF, P., TIAN, L., PAN, T., LI, R., KHINE, M., KIM, J. & WANG, J. 2018 Wearable sensors: modalities, challenges, and prospects. *Lab on a Chip* 18 (2), 217–248.
- HOLTSMARK, J., JOHNSEN, I., SIKKELAND, T. & SKAVLEM, S. 1954 Boundary layer flow near a cylindrical obstacle in an oscillating, incompressible fluid. *J. Acoust. Soc. Am.* **26** (1), 26–39.
- HUANG, H.-W., USLU, F.E., KATSAMBA, P., LAUGA, E., SAKAR, M.S. & NELSON, B.J. 2019 Adaptive locomotion of artificial microswimmers. *Sci. Adv.* 5 (1), eaau1532.
- JACOB, C., TINGAY, D.G. & LEONTINI, J.S. 2021 The impact of steady streaming and conditional turbulence on gas transport during high-frequency ventilation. *Theor. Comput. Fluid Dyn.* **35** (2), 265–291.

- JALAL, S., VAN DE MOORTELE, T., NEMES, A., AMILI, O. & COLETTI, F. 2018 Three-dimensional steady and oscillatory flow in a double bifurcation airway model. *Phys. Rev. Fluids* 3 (10), 103101.
- KAMRIN, K. & NAVE, J.-C. 2009 An eulerian approach to the simulation of deformable solids: application to finite-strain elasticity. arXiv:0901.3799.
- KAMRIN, K., RYCROFT, C.H. & NAVE, J.-C. 2012 Reference map technique for finite-strain elasticity and fluid–solid interaction. *J. Mech. Phys. Solids* **60** (11), 1952–1969.
- KLOTSA, D., BALDWIN, K.A., HILL, R.J.A., BOWLEY, R.M. & SWIFT, M.R. 2015 Propulsion of a two-sphere swimmer. *Phys. Rev. Lett.* 115 (24), 248102.
- LANE, C.A. 1955 Acoustical streaming in the vicinity of a sphere. J. Acoust. Soc. Am. 27 (6), 1082-1086.
- LIU, R.H., YANG, J., PINDERA, M.Z., ATHAVALE, M. & GRODZINSKI, P. 2002 Bubble-induced acoustic micromixing. *Lab on a Chip* **2** (3), 151–157.
- LONGUET-HIGGINS, M.S. 1998 Viscous streaming from an oscillating spherical bubble. *Proc. R. Soc. Lond.* A **454** (1970), 725–742.
- LUTZ, B.R., CHEN, J. & SCHWARTZ, D.T. 2003 Microfluidies without microfabrication. *Proc. Natl Acad. Sci.* **100** (8), 4395–4398.
- LUTZ, B.R., CHEN, J. & SCHWARTZ, D.T. 2005 Microscopic steady streaming eddies created around short cylinders in a channel: flow visualization and stokes layer scaling. *Phys. Fluids* 17 (2), 023601.
- LUTZ, B.R., CHEN, J. & SCHWARTZ, D.T. 2006 Hydrodynamic tweezers: 1. Noncontact trapping of single cells using steady streaming microeddies. *Anal. Chem.* **78** (15), 5429–5435.
- MARMOTTANT, P. & HILGENFELDT, S. 2003 Controlled vesicle deformation and lysis by single oscillating bubbles. *Nature* **423** (6936), 153–156.
- MARMOTTANT, P. & HILGENFELDT, S. 2004 A bubble-driven microfluidic transport element for bioengineering. *Proc. Natl Acad. Sci.* **101** (26), 9523–9527.
- PARK, S.-J., et al. 2016 Phototactic guidance of a tissue-engineered soft-robotic ray. Science 353 (6295), 158–162.
- PARTHASARATHY, T., BHOSALE, Y. & GAZZOLA, M. 2020 A simple, rigorous benchmark for fully coupled flow–structure interaction algorithms. arXiv:2011.09453.
- PARTHASARATHY, T., CHAN, F.K. & GAZZOLA, M. 2019 Streaming-enhanced flow-mediated transport. J. Fluid Mech. 878, 647–662.
- POMMELLA, A., HARUN, I., HELLGARDT, K. & GARBIN, V. 2021 Enhancing microalgal cell wall permeability by microbubble streaming flow. arXiv:2112.08519.
- RANEY, W.P., CORELLI, J.C. & WESTERVELT, P.J. 1954 Acoustical streaming in the vicinity of a cylinder. J. Acoust. Soc. Am. 26 (6), 1006–1014.
- SOMEYA, T., BAO, Z. & MALLIARAS, G.G. 2016 The rise of plastic bioelectronics. *Nature* **540** (7633), 379–385.
- SPELMAN, T.A. & LAUGA, E. 2017 Arbitrary axisymmetric steady streaming: flow, force and propulsion. *J. Engng Maths* **105** (1), 31–65.
- THAMEEM, R., RALLABANDI, B. & HILGENFELDT, S. 2016 Particle migration and sorting in microbubble streaming flows. *Biomicrofluidics* **10** (1), 014124.
- THAMEEM, R., RALLABANDI, B. & HILGENFELDT, S. 2017 Fast inertial particle manipulation in oscillating flows. *Phys. Rev. Fluids* **2** (5), 052001.
- Towns, J., et al. 2014 XSEDE: accelerating scientific discovery. Comput. Sci. Engng 16 (5), 62-74.
- WANG, C., JALIKOP, S.V. & HILGENFELDT, S. 2011 Size-sensitive sorting of microparticles through control of flow geometry. *Appl. Phys. Lett.* **99** (3), 034101.